AEROELASTIC ANALYSIS OF NREL WIND TURBINE

Yaozhi Lu*
Imperial College London
London SW7 2AZ, UK
Email: yaozhi.lu14@ic.ac.uk

Fanzhou Zhao
Imperial College London
London SW7 2AZ, UK
Email: fanzhou.zhao11@ic.ac.uk

Loic Salles
Imperial College London
London SW7 2AZ, UK
Email: l.salles@ic.ac.uk

Mehdi Vahdati
Imperial College London
London SW7 2AZ, UK
Email: m.vahdati@ic.ac.uk

ABSTRACT

The current development of wind turbines is moving toward larger and more flexible units, which can make them prone to fatigue damage induced by aeroelastic vibrations. The estimation of the total life of the composite components in a wind turbine requires the knowledge of both low and high cycle fatigue (LCF and HCF) data. The first aim of this study is to produce a validated numerical model, which can be used for aeroelastic analysis of wind turbines and is capable of estimating the LCF and HCF loads on the blade. The second aim of this work is to use the validated numerical model to assess the effects of extreme environmental conditions (such as high wind speeds) and rotor over-speed on low and high cycle fatigue.

Numerical modelling of this project is carried out using the Computational Fluid Dynamics (CFD) & aeroelasticity code AU3D, which is written at Imperial College and developed over many years with the support from Rolls-Royce. This code has been validated extensively for unsteady aerodynamic and aeroelastic analysis of high-speed flows in gas turbines, yet, has not been used for low-speed flows around wind turbine blades. Therefore, in the first place the capability of this code for predicting steady and unsteady flows over wind turbines is studied. The test case used for this purpose is the Phase VI wind turbine from the National Renewable Energy Laboratory (NREL), which has extensive steady, unsteady and mechanical measured data.

From the aerodynamic viewpoint of this study, AU3D results correlated well with the measured data for both steady and unsteady flow variables, which indicated that the code is capable of calculating the correct flow at low speeds for wind turbines.

The aeroelastic results showed that increase in crosswind and shaft speed would result in an increase of unsteady loading on the blade which could decrease the lifespan of a wind turbine due to HCF. Shaft overspeed leads to significant increase in steady loading which affects the LCF behaviour. Moreover, the introduction of crosswind could result in significant dynamic vibration due to forced response at resonance.

INTRODUCTION

Due to the uncertainties and risks associated with the price of fossil fuel, investment in low-emission renewable energy sources such as wind power, as a stable and long term alternative, has been increasing in the energy sector [1] [2]. However, it has been observed that the lifespan of wind turbines fall short of their design intent [3], which lowers the economic gain. Extreme environmental conditions (such as high wind speed) or control failures (such as overspeed) can result in wind turbines operating at off-design operating conditions. Such scenarios can

lead to higher than designed steady and unsteady loading, which can result in Low Cycle Fatigue (LCF) and High Cycle Fatigue (HCF) problems [3]. The current development trend of wind turbines is moving towards larger blades which could exacerbate such aeroelastic stability issues. Therefore, accurate prediction of aeroelastic behaviour of a wind turbine is vital.

Traditional aeroelastic analysis of wind turbines usually adopts the Blade Element Momentum (BEM) method [4]. Provided there is sufficiently accurate 2D airfoil data (and corrections for 3D effects [5]), the BEM method could generate relatively accurate prediction of aeroelastic load in a relatively short period of time compared to that for CFD (which is in the range of hours for the method used in this project) and thus is an ideal tool to be used in the early design stage. However, it is known that BEM experiences difficulties in modelling the tip and root regions. Besides, the steady state nature of BEM computation means it could not fully capture the dynamic loading behaviour on the wind turbine blades [5]. Hence, there exists a discrepancy between real performance and those predicted by BEM.

Due to increasing computer processing speed and capacity, there is growing interest in using CFD method and possibilities exist where CFD method could eventually replace the BEM method for aeroelasticity analysis. As mentioned by Hansen and Madsen [6], the dawn of using CFD in calculating aerodynamic load was brought by experimental cases [7–9] on NREL Phase VI rotor whose data were used by researchers [10, 11] for code validation and results comparison purpose. These data will also be used for comparison on this particular study.

The most recent effort on Fluid Structure Interaction (FSI) modelling of full scale wind turbines were from Bazilevs et al [12, 13]. A fully coupled approach where the fluid and structural domain are solved simultaneously was employed. Variable multiscale version of the Arbitrary Lagrangian-Eulerian method is adopted to resolve the fluid domain while the structural domain is governed by the Kirchhoff-Love shell theory. The study on the NREL 5MW wind turbine demonstrates the importance of a coupled approach in predicting the its behaviour [12, 13].

The aeroelastic solver used for this study, AU3D, is an unsteady, 3D compressible Navier-Stokes solver which can use structured, unstructured, or hybrid grids, and has a moving grid capability for aeroelastic analysis. The aeroelastic computations are based on a time-accurate non-linear FE formulation of the structure, which is moved according to the aerodynamic forces acting on the body. AU3D has been validated extensively for unsteady aerodynamic and aeroelastic analysis of high-speed flows in gas turbines, but, has not been used for low-speed flows around wind turbine blades. The aims of this study are to first validate the aeroelastic solver's capability in predicting wind turbine aerodynamic performance and then to investigate wind turbine aeroelastic behaviour at extreme conditions.

This paper is outlined as follows. Firstly, the aerodynamic and aeroelastic models used by the solver AU3D are introduced. Secondly, aerodynamic validation of the solver is presented to establish confidence in the solver in the prediction of fluid behaviour around 2D airfoil and 3D wind turbine. Finally, the validated solver is used rather like an experimental tool to investigate wind turbine blade behaviour under extreme conditions such as shaft overspeed and high crosswind.

TEST CASE: NREL PHASE VI WIND TURBINE

The National Renewable Energy Laboratory (NREL) conducted a series of Unsteady Aerodynamics Experiments (UAE) tests on wind turbines in the NASA-Ames wind tunnel [8]. The NREL Phase VI wind turbine tested at NASA-Ames wind tunnel was a two-bladed, 10-metre rotor diameter stall-regulated Horizontal-Axis Wind Turbine (HAWT). Both upwind and downwind configurations were tested as well as various yaw and blade tip pitch angles. Pressures distributions on the blade surfaces, shaft torque, thrust, and the root flapwise and edgewise bending moments were measured by means of blade mounted sensors and pressure taps.

The blades of the NREL Phase VI wind turbine are constructed using the S809 aerofoil designed specifically for HAWT applications [14]. The S809 aerofoil has a thickness of 21% chord length with primary objectives of restrained maximum lift, insensitivity to leading edge roughness, and low profile drag [14, 15]. Experimental tests of the S809 aerofoil were conducted by Delft University of Technology at its low speed laboratory on a 2D blade section of 0.6m chord. Characteristics of the S809 aerofoil, including pressure distributions and aerodynamic force coefficients, were recorded and documented in Somers [14].

AERODYNAMIC MODEL

The CFD computations conducted in this study are based on a 3D, time-accurate, viscous, finite-volume compressible flow solver [16]. The unsteady flow cases are computed using the Unsteady Reynolds-Averaged Navier-Stokes (URANS) equations, with the basic assumption that the frequencies of interest are sufficiently far away from the frequencies of turbulent flow structures (in boundary layer). The flow variables are represented on the nodes of a generic unstructured grid and numerical fluxes are computed along the edges of the grid. The numerical fluxes are evaluated using Roe's flux vector difference splitting to provide matrix artificial dissipation in a Jameson-Schmidt-Turkel (JST) scheme [17]. The overall solution method is implicit, with second-order accuracy both spatially and temporally. For steady-state flow computations, the solution is advanced in pseudo-time using local time stepping, while dual time stepping is used for unsteady computations to preserve time accuracy. For steady-state flow calculations, solution acceleration techniques such as residual smoothing and local time stepping are employed. The current computations use the one-equation Spalart-Allmaras tur-

bulence model [18]. The parameters in Spalart-Allmaras have been adjusted for high speed fan blades in aero engines to attain good agreement near the stability limit; the parameters are held constant in all the present computation. The resulting CFD code has been used over the past 20 years for flows at off design conditions with a good degree of success [19–21].

AEROELASTIC MODEL

The aeroelastic analysis in AU3D is performed in a partially coupled fashion [22] in which fluid and structural domain are solved alternately with data exchanged at the fluid structure boundary at each time step. The underlying assumption of this aeroelastic model is that the structural motion could be represented by linear superposition of a few fixed modes [23]. Mode shapes for aeroelastic analysis are obtained from the FE package ANSYS Mechanical and are interpolated onto the CFD grid. The mode shapes remain fixed during computation based on the assumption that the mechanical mode is unaffected by the aerodynamic forces. This aeroelastic solution approach differs from the fully coupled analysis as the FE analysis is not conducted during each time step and hence it is computationally less demanding.

Aeroelastic computation starts by solving Equation (1) for each mode [24].

$$[M]\{\ddot{x}\} + [C]\{\dot{x}\} + [K]\{x\} = \{F\} \tag{1}$$

where $[M]$,$[C]$, and $[K]$ are mass, damping, and stiffness matrices respectively. $\{x\}$ and $\{F\}$ are vectors of displacements and forces respectively. Due to the low rotor speed of the wind turbine, the resultant centrifugal force, and consequently the centrifugal stiffening effect, is negligible compared to the aerodynamic loading and thus the force vector only includes the aerodynamic loading. In fact, it is found through structural modelling that modal frequencies experience a less than 2% change between static condition and running condition (72 RPM). Likewise, the geometry does not include the deformation induced by centrifugal force. To convert the spatial model to the modal model, displacement $\{x\}$ is transformed into the product of mass-normalized mode shape $[\Phi]$ and modal displacement $\{q\}$ [22, 23].

$$\{x\} = [\Phi]\{q\} \tag{2}$$

Using the orthogonality properties of the modal model [25]:

$$[\Phi]^T[M][\Phi] = [I] \tag{3}$$

$$[\Phi]^T[K][\Phi] = \begin{bmatrix} \diagdown & \\ & \omega_n^2 \\ & & \diagdown \end{bmatrix} \tag{4}$$

where ω_n is the modal frequency.The terms on the right hand side of Equation (3) and (4) are the identity matrix and diagonal matrix of squared natural frequencies respectively. Thus, equation (1) could be transformed into:

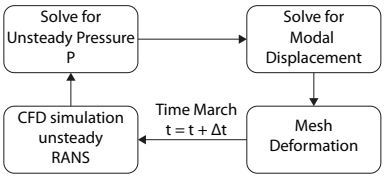

FIGURE 1: Aeroelastic model solution scheme.

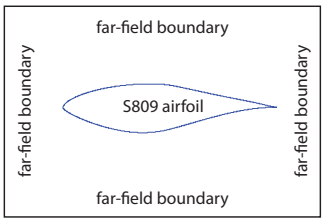

FIGURE 2: Domain of steady state computations (not to scale).

$$\{\ddot{q}\} + \begin{bmatrix} \diagdown & \\ & 2\zeta\omega_n \\ & & \diagdown \end{bmatrix}\{\dot{q}\} + \begin{bmatrix} \diagdown & \\ & \omega_n^2 \\ & & \diagdown \end{bmatrix}\{q\} = [\Phi]^T\{F\} \tag{5}$$

Results from FE modelling will provide information about the two diagonal matrix on the left hand side and the mass-normalised mode shape on the right hand side. The vector $\{F\}$ represents the aerodynamic forces acting on the blade and is obtained from a CFD code (i.e. AU3D). The term on the right hand side of Equation (5) is the modal force which is a measure of the correlation between the aerodynamic force and the mode shape in that particular mode.

After obtaining the aerodynamic forces $\{F\}$ at time level n, the aeroelastic solver computes the modal displacement $\{q\}$ from Equation (5) which is used to calculate the real displacement $\{x\}$ on the blade surface mesh at time level $n+1$ from Equation (2). The mesh on blade surface is deformed every time step by the imposed modes using mode shapes and modal frequencies. Boundary condition at the fluid-structure interface is updated at each time step [24] as illustrated in Figure 1. Hence, the deformed mesh will be used in the next time step in CFD simulation. The physical time step for aeroelastic computations is assigned as approximately 800 time steps per revolution. This time step setting was determined by performing a temporal convergence study.

AERODYNAMIC VALIDATION

2D Validation: S809 aerofoil

Figure 2 illustrates the domain of CFD computations for the S809 aerofoil. The far-field boundaries are placed approximately 60 chords away from the aerofoil so as to minimise the effect on the near blade flow field. The overall grid is unstructured, with hexahedral elements around the aerofoil in the boundary layer

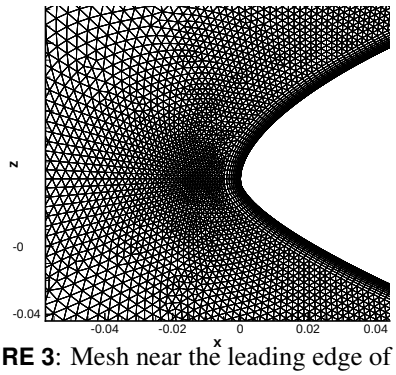

FIGURE 3: Mesh near the leading edge of the aerofoil.

region and prismatic elements in the rest of the domain. Figure 3 shows the mesh around the leading edge. The overall grid contains approximately 313,000 mesh points with 1,880 nodes on the surface of the aerofoil.

Steady state flow solutions are obtained by imposing flow velocities, static pressure and static temperature at the far-field boundaries. The variation in Angle of Attack (AOA) is achieved by changing the free-stream flow angle at the far-field boundaries. In this study, the angle of attack is varied between -0.01° and 20.15°. All the computations are performed in a fully turbulent manner with a Reynolds number of 1×10^6.

Figure 4 shows the comparison of pressure distribution on the aerofoil surface between the experimental measurements and the results obtained from CFD computations. In this figure the results for four different AOAs are displayed: -0.01°, 5.13°, $9.22^\circ$and 14.24°. At -0.01° AOA (red curve and symbols in Figure 4a), the calculated pressure distribution shows good agreement with the experimental data. Small discrepancies can be seen at about $x/c = 0.55$ on the suction surface, which is attributed to the laminar separation bubbles observed in the experiments [14]. The laminar/turbulent transition is not modelled in this study as the computations were performed in a fully turbulent manner. For AOA of 5.13°(blue curve and symbols in Figure 4a), it is seen that the static pressure is slightly over-predicted in the forward half of the suction surface. This over-prediction of pressure coefficient was also observed in [26–29]. With the increase in AOA (Figure 4b), the over-prediction of static pressure in the forward half of the suction surface becomes more noticeable. Again, this discrepancy is likely due to the fact that a transitional flow is being compared against a . Nevertheless, the predicted pressure distribution on the aerofoil shows good agreement with the experimental measurements. Again, this discrepancy is likely due to the fact that a simulated turbulent flow is being compared to a transitional flow in reality. Nevertheless, the predicted pressure distribution on the aerofoil shows good agreement with the experimental measurements.

Figure 5 shows the comparison of lift coefficient (c_l) between the experimental measurements (symbols) and the results

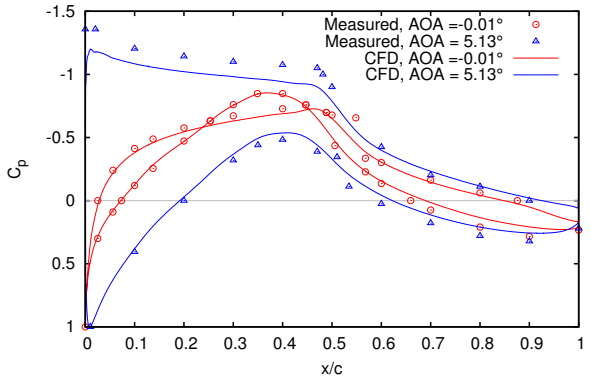

(a)

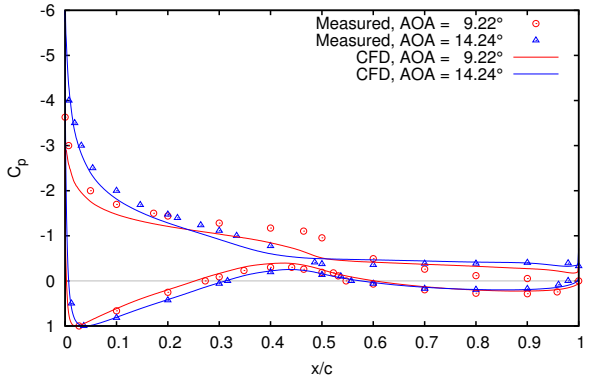

(b)

FIGURE 4: Pressure distribution on the surface of the aerofoil.

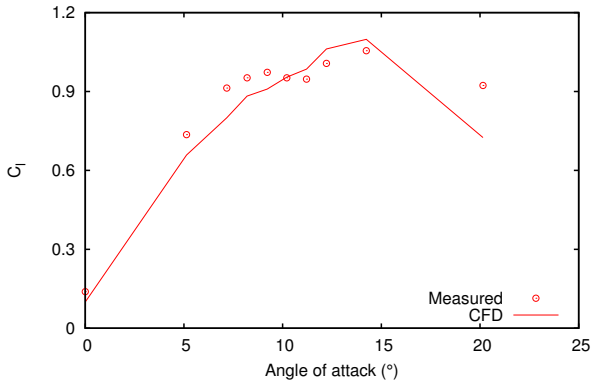

FIGURE 5: Lift coefficient as a function of angle of attack.

obtained from CFD computations (solid curve) as a function of AOA. For AOA less than 10°, the lift coefficient is slightly under-predicted, which is attributed to the slight over-prediction of static pressure in the forward half of the suction surface as observed in Figure 4. The measured lift coefficient shows a small decrease at about 9.22°AOA, which is driven by the onset of flow separation on the suction surface [26, 30]. This trend is adequately captured by the CFD model where a decrease in the slope

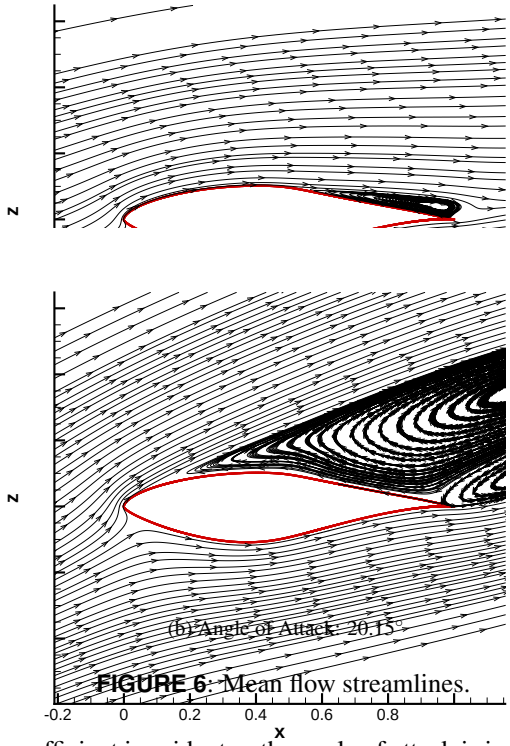

FIGURE 6: Mean flow streamlines.

of lift coefficient is evident as the angle of attack is increased beyond 8.20°. This phenomenon is clearly demonstrated by the mean flow streamline plot in Figure 6a for 8.20°AOA, where separated flow can be identified on the suction surface near the trailing edge. The aerofoil stalls at approximately 14.24°AOA due to the expansion of separated flow on the suction surface, which manifests as a decrease in the lift coefficient as the angle of attack is increased. This trend is well captured by the CFD code. Figure 6b shows instantaneous mean flow streamlines for 20.15°angle of attack calculated using CFD. The stalling of the aerofoil can be clearly identified from the streamline plot, where flow separation occurs on the suction surface just aft the leading edge. It should be noted that due to large scale flow separation and the consequent unsteadiness, the lift coefficient for 20.15°AOA shown in Figure 5 represents the time-averaged value. The under-prediction of lift coefficient at 20.15°AOA is believed to be the result of over-estimated separation vortices on the suction surface of the aerofoil. Overall, the lift coefficient calculated using CFD shows good agreement with the experimental measurements, and similar trends are observed when compared with other RANS CFD studies [26, 27, 31].

Figure 7 shows the comparison of drag coefficient (c_d) between the experimental measurements (symbols) and the results obtained from CFD computations (solid curve) as a function of angle of attack. The predicted drag coefficient shows good agreement with the measured data. The slight over-prediction at low AOA (less than 10°) is linked to the under-estimation of lift coefficient as observed in Figure 5. The local peak of drag coefficient at 11.21°, driven by the onset of flow separation at 9.22°, is not captured by the CFD model. This discrepancy was also observed by [26, 27, 31] despite the use of SST $k-\omega$ turbulence model which is known to be suitable for flow conditions with adverse

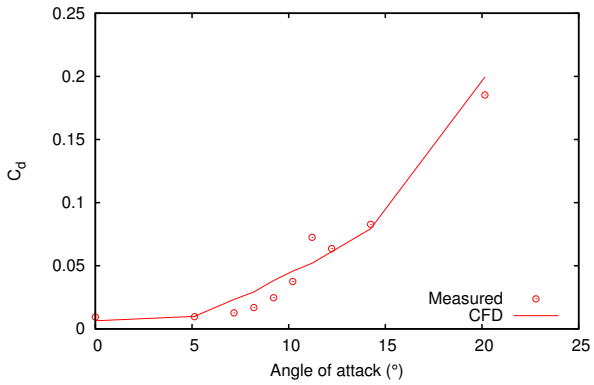

FIGURE 7: Drag coefficient as a function of angle of attack.

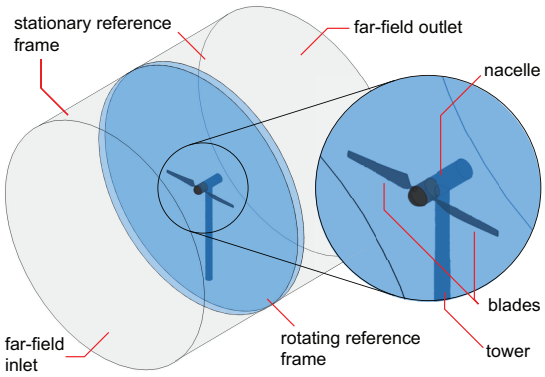

FIGURE 8: Aerodynamic/aeroelastic computation domain.

pressure gradients. The findings indicate that there is still room for improvements regarding the turbulence model in the present RANS based CFD solvers on the matter of stall inception for two-dimensional aerofoils in low speed flows. However, Figure 5 and 7 show that the aerodynamic forces on the blade which is the most important parameter for aeroelastic analysis, are adequately predicted by the current CFD code.

3D Validation: Phase VI wind turbine

The results in the previous section clearly demonstrate the capability of AU3D in predicting the aerodynamic performance of the S809 aerofoil. In the next step, validation of the code is carried out by comparing the aerodynamic performance of the NREL Phase VI wind turbine calculated using CFD and obtained through experimental measurements.

Figure 8 shows the model of the NREL Phase VI wind turbine and the computation wind tunnel domain used in this study. The main bodies of the turbine blades are constructed based on a series of constant span aerofoil sections (25% to 100% span) [9]. The exact geometry for the blade root, tip and the nacelle are not specified in the experimental report [9], thus simple geometries are assumed to avoid unnecessary artificial complexities. A lin-

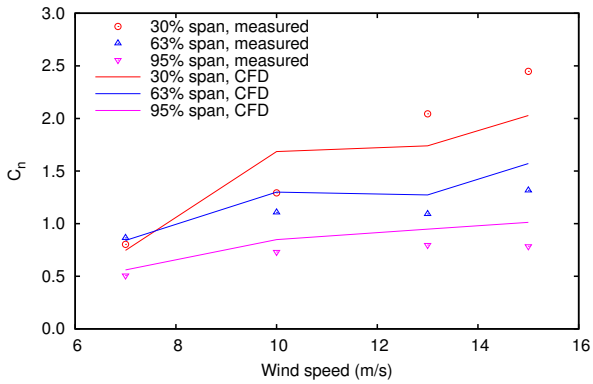

FIGURE 9: Normal force coefficient as a function of wind speed.

ear transition is adopted from the cylindrical blade root to the aerofoil section at 25% span. The tip section (100% span) is treated as flat end, and the nacelle is modelled as a cylindrical body with a hemisphere hub. Initial azimuth angle for the blade on the left hand side in Figure 8 is set to 90° (in NREL reference frame [9]).

The domain of CFD computation consists of a cylindrical wind tunnel, with far-field boundaries placed (axially and radially) approximately three blade radii away from the centre of the nacelle. The computation domain is split into rotating and stationary domains, where the rotating domain (blue region in Figure 8) contains the turbine blades and part of the nacelle section. The stationary domain consists of the volume downstream of hte blade with tower and the volume upstream of the blade. The boundary between rotating and stationary domains is modelled as sliding plane.

The grid for the fluid domain is constructed using the commercial package Gambit. A fully unstructured tetrahedra grid is generated which allows conformance to the non-axisymmetric blade and tower assembly. The constant span blade section mesh is similar to that shown in Figure 3. Away from the wind turbine, the mesh is gradually coarsened which results in mixing.

CFD computations are performed by imposing flow velocities, static pressure and static temperature at the far-field inlet and outlet boundaries. Unsteady computations are carried out at the wind speeds of 7 m/s, 10 m/s, 13 m/s and 15 m/s with 0° yaw angle. Aerodynamic coefficients for the forces on the turbine blades, namely the normal force coefficient c_n, pitching moment coefficient c_m, torque coefficient c_{tq} and thrust coefficient c_{th}, are calculated at different constant span sections. For more information regarding the definitions of these coefficients the reader is referred to Hand et al [9]. The aforementioned aerodynamic coefficients are shown in Figure 9 to Figure 13, where the time-averaged results (over one shaft revolution) obtained from unsteady CFD computations are compared with the experimental measurements.

Figure 9 shows the comparison of normal force coefficient

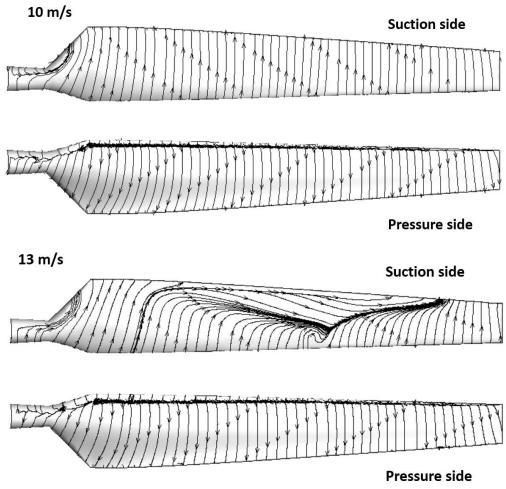

FIGURE 10: Streamline on blade surfaces.

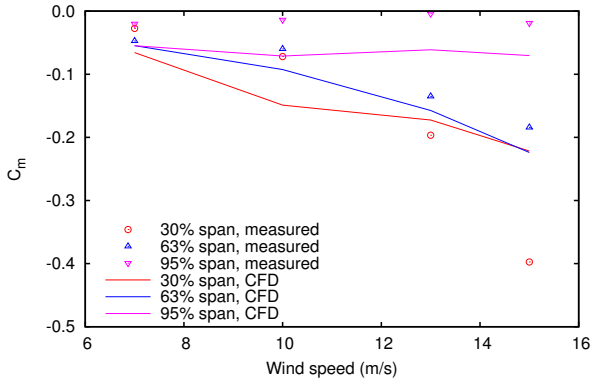

FIGURE 11: Pitching moment coefficient as a function of wind speed.

as a function of wind speed. In general, a good agreement can be seen between the experimental measurements and the results obtained from time-averaged CFD solutions. The discrepancy at 30% span is driven by the over-estimation of the outboard flow migration on the suction surface of the blades. This is clearly shown by the isentropic surface streamline plots in Figure 10, where significant radial flow component can be identified as the wind speed is increased above 10 m/s.

Figure 11 shows the comparison of pitching moment coefficient as a function of wind speed. The calculated pitching moment coefficient shows adequate agreement with the experimental measurements. Despite the slight over-prediction in magnitude, the overall trend agrees reasonably well for the 95% span and 63% span sections. The discrepancy at 30% span is again believed to be the result of premature migration and separation of flow on the suction surface as identified in Figure 9 and Figure 10. The discrepancy could also be due to the difference in geometry between CFD model (where the transition between blade

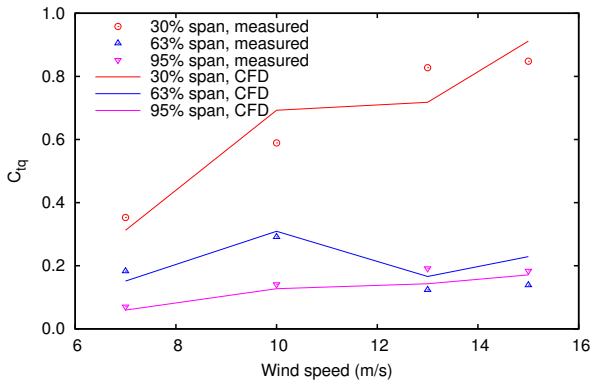

FIGURE 12: Torque coefficient as a function of wind speed.

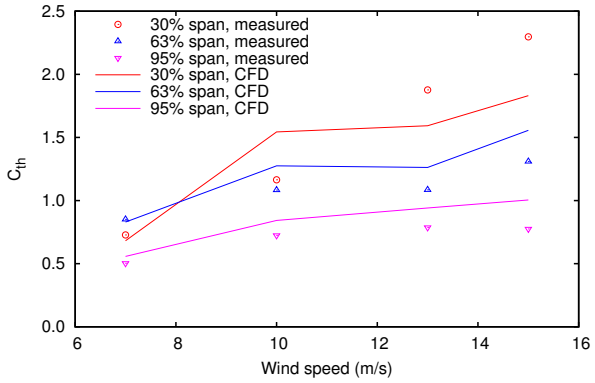

FIGURE 13: Thrust coefficient as a function of wind speed.

root and hub is assumed to be linear) and physical model.

Figure 12 and 13 show the calculated torque and thrust coefficients as a function of wind speed for the three constant span sections. A good agreement with the measured data can be seen at 95% span and 63% span for all wind speeds. The stalling of the 63% span section at the wind speed of 13 m/s is clearly captured by the CFD computations. The premature stall at 30% span again results in noticeable discrepancies between the CFD computations and the experimental measurements.

Figure 14 to Figure 16 show the calculated pressure distribution at 30%, 63% and 95% span of the blade for two wind speeds: 10 m/s and 13 m/s. As can be seen from the plots, the pressure distribution calculated using CFD show very good agreement with the measured data at 95% span and 63% span. On the other hand, the calculated flow at 30% span shows differences from the measured data for wind speeds above 10 m/s, where flow separation on the suction surface is over-estimated leading to the loss of aerodynamic performance as observed in the previous plots.

Overall, the aerodynamic performance of the wind turbine is calculated with good degree of accuracy using the CFD model. Noticeable discrepancies at 30% span are likely due to the results of over-estimated boundary layer thickening, which leads

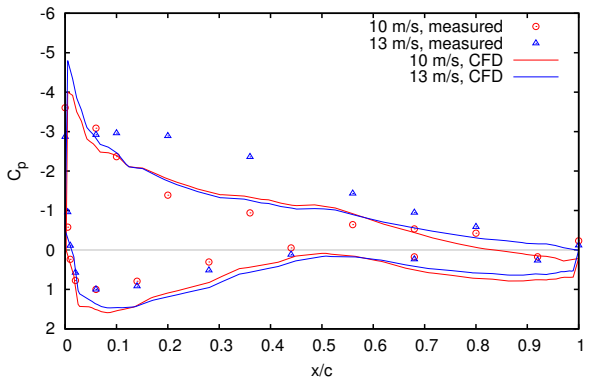

FIGURE 14: Pressure distribution at 30% span of the blade.

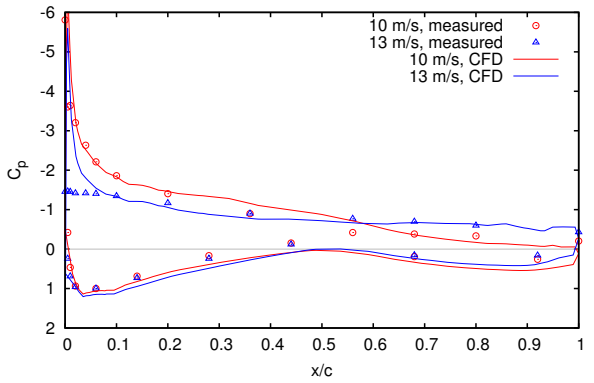

FIGURE 15: Pressure distribution at 63% span of the blade.

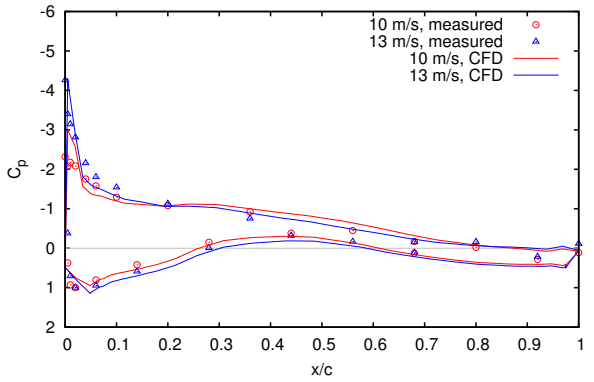

FIGURE 16: Pressure distribution at 95% span of the blade.

to premature migration and separation of the flow on the suction surface, and the lack of realistic geometry at the root of the turbine blades (below 25% span). The results show a good agreement between the CFD results and measured data for the force and pitching moment on the blade, especially at higher radial positions. This is important from an aeroelastic view point as the maximum displacement occurs at the high span locations of the blade and hence accurate modelling of the forces in these regions

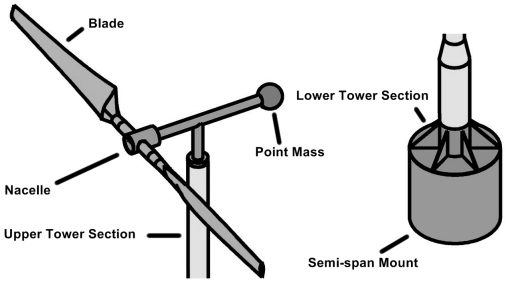

FIGURE 17: Structural domain (not to scale).

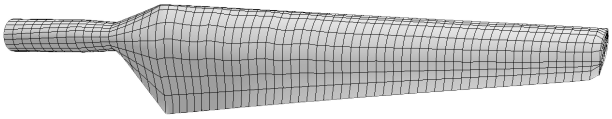

FIGURE 18: Blade FE mesh.

is crucial.

STRUCTURAL MODELLING

Figure 17 shows the geometry of the wind turbine used for the FE analysis. The contact regions between components were modelled as bonded - neither separation nor sliding were allowed. Available data on the nacelle region only consist of total mass and moment of inertia about yaw axis/tower axis. It was found that both requirements could not be satisfied simultaneously by using generic geometry and homogeneous material property. Therefore, it was decided to use a simplified geometry with aluminium and a point mass at the back (shown in Figure 17) to satisfy the moment of inertia condition. As this setup only matches the moment of inertia with respect to one of the three axis, modes involving rotation with respect to the other two axis are expected to have errors. From the modal frequency data obtained, it is found that the FE simulation does not have all the modes and the existing modal frequencies show significant disagreement with experimental results as expected. Measures used to minimise the negative influence of the inaccuracies incurred in structural side of the study are discussed in the next section.

Due to the nature of geometrical and structural data provided by NREL, it was deduced that the most efficient way to conduct modal analysis on turbine blade would be to model it as a 3D solid body (though the actual blade is hollow) with homogeneous material property. Figure 18 shows the FE mesh on the surface of the blade. This is a simplified approach since the material is only present on part of the blade section [9] and hence is likely to results in errors in FE modelling.

As the exact match of vibration modes between the FE results and the measured data is unlikely, the identification of modes were achieved based on the correlation between the modal displacement obtained from the FE analysis and the measured

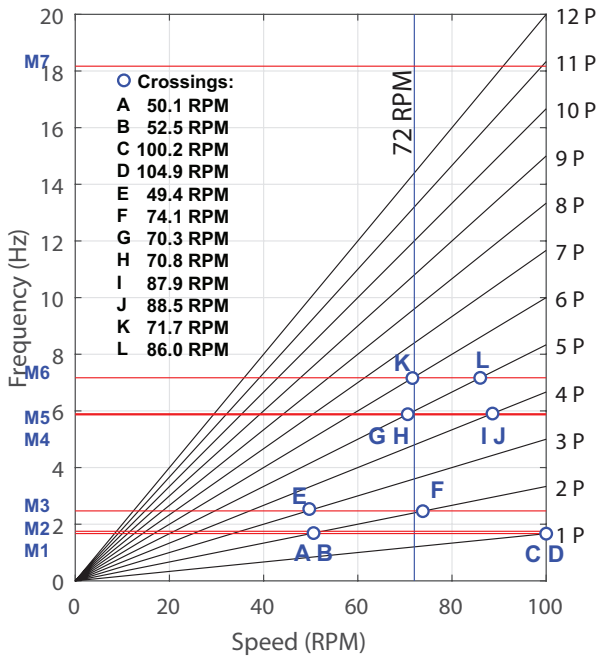

FIGURE 19: Campbell diagram.

strain gauge data [9]. Figure 19 shows the Campbell diagram for the wind turbine, in terms of frequency against rotor shaft speed, where the first 7 identified modes (M1 to M7) are illustrated. Also shown in this figure are the vertical line marking the design speed of the wind turbine (72 RPM) and the harmonics of blade-tower passing (1P, 2P, etc). At the crossings between the lines of blade-tower passing harmonics (black lines) and the lines of natural frequency of vibration modes (red lines), synchronous vibration (aka forced response) occurs where the motion of the blade is excited by the periodic forcing due to the flow field distortion. In such situations, the vibration levels of the blade depend on the magnitude of flow field distortion, and the correlation between the unsteady pressure and the blade vibration mode (i.e. modal force). High levels of unsteady aerodynamic loading, and consequently large amplitude blade vibrations, can result in high cycle fatigue of wind turbine blades which shortens the life span and limits the economic gain.

The crossings of interest in this study, in other words the conditions at which forced response is most likely a threat to the rotor stability, are illustrated by the circular symbols in Figure 19. Two crossings are identified in the vicinity of the design speed (72 RPM): Mode 3 with 2P at 74.1 RPM, and Mode 4 with 5P at 70.8 RPM. The potential outcome of the two crossings can be described as follows: when the wind turbine is operated at the design speed, the frequency of excitation (2P or 5P) is close to the natural frequency of a blade mode (Mode 3 or 4); due to the proximity of the two frequencies, the frequency of blade vibration can 'lock in' to the frequency of excitation, giving rise to increasing unsteady loading and high vibration levels.

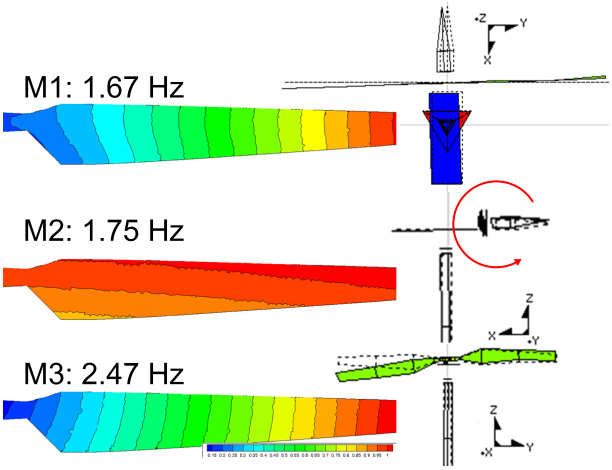

FIGURE 20: Three mode shapes used for aeroelastic computation. Left: absolute displacement contour on blade. Right: Blade behaviour captured by NREL [32].

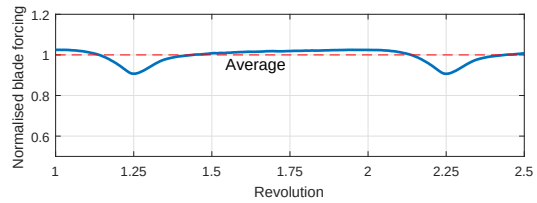

(a) Modal force time history for M2 mode

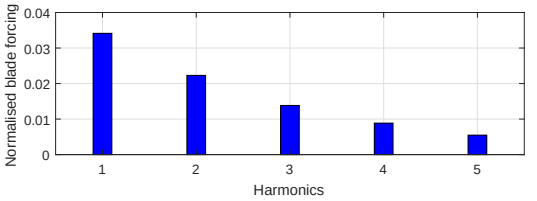

(b) FFT of modal force time history

FIGURE 21: Modal forces for M2 at 10 m/s axial speed, 0° crosswind, and 72 RPM rotation speed.

AEROELASTIC ANALYSIS

Aeroelastic computations were carried out for the first three modes at various operating conditions (such as wind speed, rotor shaft speed and crosswind), with the datum case being at the operating conditions specified by the Sequence S of the Phase VI wind turbine experiment [9]: 72 RPM shaft speed, 10 m/s free stream wind speed and 0° yaw angle (i.e. no crosswind). The blade mode shape of the first three modes are illustrated in Figure 20. For M1 the blades behaves like a flapwise bending and M3 behaves like an edgewise bending mode. M2 is extracted from a complex tower mode when the tower is moving in the axial direction. The natural frequencies of the modes were chosen to be consistent with the values measured in the experiment (as illustrated in Figure 19) [9]. For static aeroelastic analysis, critical mechanical damping is imposed on all the modes so that the equilibrium between the fluid and the structural domains can be achieved in a timely fashion.

In order to investigate the aeroelastic behaviour of the wind turbine blades at extreme off-design operating conditions, such as overspeed and strong crosswind, unsteady computations are performed by varying the rotor shaft speed, free stream wind speed and the extent of crosswind. Time history of the modal force is tracked, based on which the transient loading on the blade is obtained.

Figure 21 shows an example of the computed modal force on the blade surface for the M2 mode at a free stream wind speed of 10 m/s in the absence of crosswind. Figure 21a shows the time history of the modal force as a function of shaft revolutions, where the last two cycles computed are displayed. At this flow condition, the air induces a pitching moment about the centre line of the blade, which manifests as a non-zero mean level of modal force as shown by the dashed red line in Figure 21a. Data presented in Figure 21 are normalised against this value. In addition, the passing between the blade and the tower induces an impulsive forcing which occurs once every revolution (e.g. at 1.25 and 2.25 revolutions in Figure 21a). The level of the impulsive forcing depends on the magnitude of flow field distortion, and the correlation between the unsteady pressure and the blade vibration mode. Figure 21b shows the amplitude of harmonics for the modal force time history shown in Figure 21a, calculated based on the discrete Fourier transform for a complete shaft revolution. It is seen from Figure 21b that, the amplitude of blade-tower passing harmonics is significantly smaller than that of the steady loading (less than 3.5%). Moreover, for the case shown here, the amplitude diminishes for higher harmonics. By performing the above analysis, the steady loading and the unsteady loading on the wind turbine blade can be isolated. The LCF could be analysed through steady loading whereas HCF could be analysed through unsteady loading at the correct frequency and harmonics. Based on this analysis, potential causes for low cycle fatigue, driven by high amplitude of steady loading leading to plastic deformation, and high cycle fatigue, driven by unsteady forcing such as that induced by the blade-tower passing, are explored. These aspects are discussed in the following sections. The primary concern of this study is to investigate the trend of steady and unsteady loading variations at different conditions. Therefore, only modal force is considered.

Variations in steady force and unsteady force are illustrated in Figure 22 and 23. In these plots, the forces are normalised with respect to the reference case with 10 m/s axial velocity, 72 RPM shaft speed, and 0° yaw angle (i.e. no crosswind). Steady modal forces for M2 and M3 mode are presented. Unsteady modal forces up to 5th harmonic for M2 mode are presented. Unsteady modal forces for M3 are omitted for they are of much smaller scale as compared to the steady modal force than those from M2, meaning they are of less concern in terms of HCF.

In the rotor speed study, increases in steady and unsteady

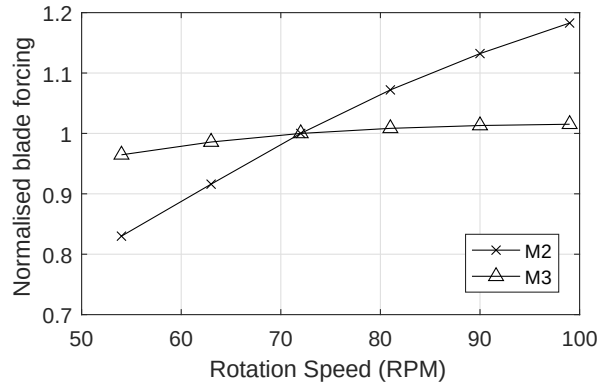

(a) Steady modal force variation

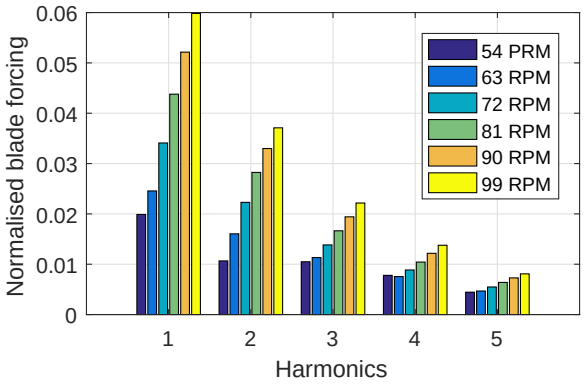

(b) Unsteady modal force variation for M2

FIGURE 22: Modal force variations with respect to shaft speed (0 crosswind and 10 m/s wind speed).

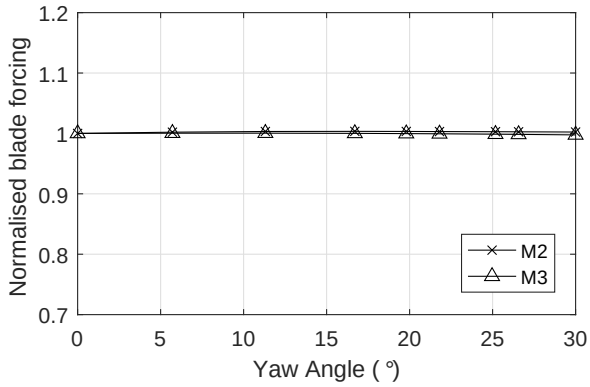

(a) Steady modal force variation

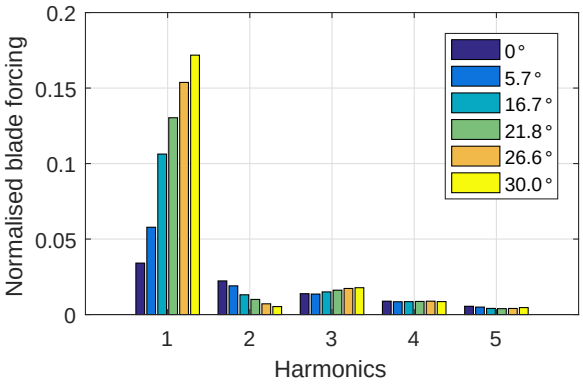

(b) Unsteady modal force variation for M2

FIGURE 23: Modal force variations with respect to yaw angle (72 RPM and 10 m/s wind speed).

modal force are observed for both M2 and M3 as the rotor speed is increased. From the steady modal force plot in Figure 22a, it is evident that M2 is significantly more sensitive to rotation speed increase than M3 is. Hence, M2 could impose substantial steady loading in an overspeed scenario and make the wind turbine susceptible to LCF. From Figure 22b, the data indicate increase in unsteady modal across all harmonics though the percentage change diminishes significantly at higher harmonics. This indicates the wind turbine becomes less resistant to HCF during overspeed as the 1^{st} harmonic loading at 99 RPM has increased by 75.5% with respect to that at the design condition of 72 RPM. Thus, an increase of 37.5% in shaft speed has led to a disproportionally higher increase in unsteady loading.

Crosswind effect was introduced by adding a free stream velocity perpendicular to both tower axis and axial direction while keeping the axial free stream velocity constant at 10 m/s. Thus, this study imitates the situation where yaw control fails to orientate the turbine in primary wind direction. The results are then presented in terms of resultant yaw angle in Figure 23. As crosswind velocity increase, negligible change is observed for the steady components. Thus, in terms of LCF, it could be inferred that the turbine is less prone to change in crosswind. In contrast, as shown in Figure 23b, the sharply increasing 1^{st} harmonic unsteady force is sufficiently high to result in high off-resonance responses. As illustrated by Figure 23b, as the resultant yaw angle increases from 0° to 30°, the unsteady modal forces has increased by four times from being 3.4% of the steady modal force at reference condition to 17.2%, leading to notable increase in vibratory motion. This is significantly higher than that shown earlier in the rotation speed study. Thus, the wind turbine is more susceptible to HCF damage from crosswind than from overspeed.

Among the increasing unsteady components, unsteady loading from the 2^{nd} harmonic has decreased while the changes above 3rd harmonic become negligible. This suggests the unsteady forcing in 1^{st} harmonic which is of the same frequency as the rotor speed becomes dominant with the introduction of crosswind. This phenomena could be explained through the resultant velocity on the blade. With the introduction of crosswind, when viewing in the rotor frame of reference, the resultant velocity vector changes as the blades rotates. Consequently, as illustrated in Figure 24, all plots converge at two points labelled A and B

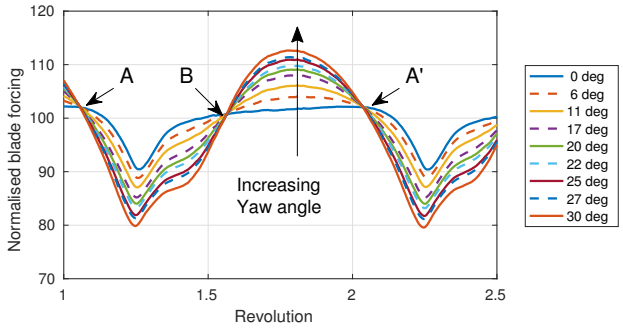

FIGURE 24: Modal force plots for M2 at various yaw angle (72 RPM and 10 m/s wind speed).

which have the same relative velocity vector. As the turbine rotates and reach blade position denoted by A once again at A', another cycle of crosswind induced periodic forcing which has the same frequency as the rotor start. Therefore, as supported by the data in Figure 23b, the 1^{st} harmonic response becomes dominant among the other harmonics. Thus, both crosswind and periodic forcing (due to tower) could enhance the unsteady loading at 1^{st} harmonic and exacerbate the wind turbine's immunity to HCF unfavourably.

The wind speed study imitates the scenario where control mechanism fails to adjust either rotation speed or pitch angle under high wind speed. The results in Figure 25 show that high wind speed makes the wind turbine more prone to LCF while causing negligible change to its HCF behaviour. Results in Figure 25b indicate a 20% increase (from 10 m/s to 12 m/s) in wind speed leading to disproportionally smaller increase in steady loading.

CONCLUSION

From the aerodynamic aspects of this study, the validation between experimental and AU3D results shows the code is capable of adequately capturing the behaviour of flow around the wind turbine. Additionally, the comparison demonstrates that the code is well equipped to model the flow at high span location which is important from an aeroelastic view point as the maximum displacement occurs at this region. By using the validated code, the modal force variations are investigated in the aeroelastic study. It is demonstrated that wind turbine is more susceptible to LCF issues under overspeed and high wind speed, whereas crosswind has negligible effect on the steady loading and thus LCF. It is more prone to HCF at overspeed and high crosswind conditions. To further this study, the next step would be to model the NREL 5MW wind turbine [33] which has comprehensive data describing the wind turbine and is widely studied by other researchers [12, 13]. Overall, this initial path finding study demonstrate the CFD and aeroelastic code AU3D is capable of FSI studies with low-speed flows around wind turbine.

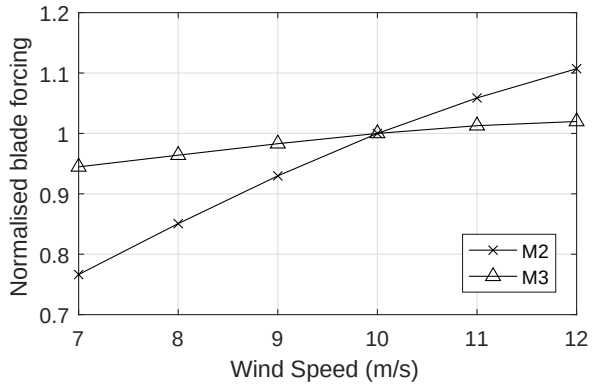

(a) Steady modal force variation

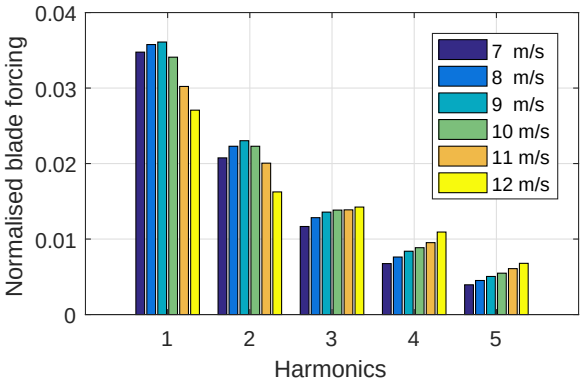

(b) Unsteady modal force variation for M2

FIGURE 25: Modal force variations with respect to wind speed (0 crosswind and 72 RPM).

ACKNOWLEDGMENT

We gratefully thank Dr Scott Schreck from NREL for providing us with raw data of the UAE project.

REFERENCES

[1] Department for Business, Energy and Industrial Stratey. Energy trends: Renewables. Available at: https://www.gov.uk/government/statistics/energy-trends-section-6-renewables. [Online; accessed 15-AUG-2016].

[2] Department for Energy and Climate Change. Deliverying uk energy investment: Low carbon energy. Available at: https://www.gov.uk/government/uploads/system/uploads/attachment_data/file/419024/DECC_LowCarbonEnergyReport.pdf. [Online; accessed 24-JAN-2017].

[3] European Wind Energy Association, 2009. *The economics of wind energy*. EWEA.

[4] Glauert, H., 1935. "Airplane propellers". In *Aerodynamic theory*. Springer, pp. 169–360.

[5] Madsen, H. A., and Rasmussen, F., 2004. "A near wake model for trailing vorticity compared with the blade element momentum theory". *Wind Energy,* ***7***(4), pp. 325–341.

[6] Hansen, M. O., and Madsen, H. A., 2011. "Review paper on wind turbine aerodynamics". *Journal of fluids engineering,* ***133***(11), p. 114001.

[7] Fingersh, L. J., Simms, D., Hand, M., Jager, D., Cotrell, J., Robinson, M., Schreck, S., and Larwood, S., 2001. "Wind tunnel testing of NREL unsteady aerodynamics experiment". *AIAA paper,* ***35***, p. 2001.

[8] Simms, D. A., Schreck, S., Hand, M., and Fingersh, L., 2001. NREL unsteady aerodynamics experiment in the NASA-Ames wind tunnel: a comparison of predictions to measurements. NREL/TP-500-29494. Tech. rep., NREL.

[9] Hand, M. M., Simms, D., Fingersh, L., Jager, D., Cotrell, J., Schreck, S., and Larwood, S., 2001. Unsteady aerodynamics experiment Phase VI: wind tunnel test configurations and available data campaigns. NREL/TP-500-29955. Tech. rep., NREL.

[10] Sørensen, N. N., Michelsen, J., and Schreck, S., 2002. "Navier–stokes predictions of the NREL Phase VI rotor in the NASA Ames 80 ft× 120 ft wind tunnel". *Wind Energy,* ***5***(2-3), pp. 151–169.

[11] Duque, E. P., Burklund, M. D., and Johnson, W., 2003. "Navier-Stokes and comprehensive analysis performance predictions of the NREL Phase VI experiment". *Journal of Solar Energy Engineering,* ***125***(4), pp. 457–467.

[12] Bazilevs, Y., Hsu, M.-C., Kiendl, J., Wüchner, R., and Bletzinger, K.-U., 2011. "3D simulation of wind turbine rotors at full scale. Part II: Fluid-structure interaction modeling with composite blades". *International Journal for Numerical Methods in Fluids,* ***65***(1-3), pp. 236–253.

[13] Bazilevs, Y., Takizawa, K., Tezduyar, T. E., Hsu, M.-C., Kostov, N., and McIntyre, S., 2014. "Aerodynamic and fsi analysis of wind turbines with the ale-vms and st-vms methods". *Archives of Computational Methods in Engineering,* ***21***(4), pp. 359–398.

[14] Somers, D., 1997. Design and experimental results for the S809 airfoil. NREL/SR-440-6918. Tech. rep., NREL.

[15] Tangler, J. L., and Somers, D. M., 1995. NREL airfoil families for HAWTs. NREL/TP-442-7109. Tech. rep., NREL.

[16] Sayma, A. I., Vahdati, M., Sbardella, L., and Imregun, M., 2000. "Modeling of three-dimensional viscous compressible turbomachinery flows using unstructured hybrid grids". *AIAA Journal,* ***38***(6), June, pp. 945–954.

[17] Swanson, R., and Turkel, E., 1992. "On Central-Difference and Upwind Schemes". *Journal of Computational Physics,* ***101***(2), August, pp. 292–306.

[18] Spalart, P., and Allmaras, S., 1992. "A one-equation turbulence model for aerodynamic flows". In 30th Aerospace Sciences Meeting and Exhibit, AIAA.

[19] Vahdati, M., Simpson, G., and Imregun, M., 2011. "Mechanisms for Wide-Chord Fan Blade Flutter". *Journal of Turbomachinery,* ***133***(4), p. 041029.

[20] Choi, M., Smith, N. H. S., and Vahdati, M., 2013. "Validation of Numerical Simulation for Rotating Stall in a Transonic Fan". *Journal of Turbomachinery,* ***135***(2), p. 021004.

[21] Dodds, J., and Vahdati, M., 2014. "Rotating Stall Observations in a High Speed Compressor Part II: Numerical Study". *Journal of Turbomachinery,* ***137***(5), p. 051003.

[22] Sayma, A., Vahdati, M., and Imregun, M., 2000. "An integrated nonlinear approach for turbomachinery forced response prediction. Part I: Formulation". *Journal of Fluids and Structures,* ***14***(1), pp. 7 – 101.

[23] Marshall, J., and Imregun, M., 1996. "An analysis of the aeroelastic behavior of a typical fan-blade with emphasis on the flutter mechanism". *ASME Paper No. 96-GT-78*.

[24] Vahdati, M., Simpson, G., and Imregun, M., 2011. "Mechanisms for wide-chord fan blade flutter". *Journal of Turbomachinery,* ***133***(4), p. 041029.

[25] Ewins, D., 1984. *Modal Testing: Theory and Practice*. Mechanical engineering research studies: Engineering dynamics series. Research Studies Press.

[26] Wolfe, W., and Ochs, S., 1997. "CFD calculations of S809 aerodynamic characteristics". In 35th Aerospace Sciences Meeting and Exhibit, p. 973.

[27] Guerri, O., Bouhadef, K., and Harhad, A., 2006. "Turbulent flow simulation of the NREL S809 airfoil". *Wind Engineering,* ***30***(4), pp. 287–301.

[28] Yang, S., Chang, Y., and Arici, O., 1994. "Incompressible navier-stokes computation of the NREL airfoils using a symmetric total variational diminishing scheme". *Journal of solar energy engineering,* ***116***(4), pp. 174–182.

[29] Chang, Y., Yang, S., and Arici, O., 1996. Flow field computation of the NREL S809 airfoil using various turbulence models. Tech. rep., ASME.

[30] Le Pape, A., and Gleize, V., 2006. "Improved Navier-Stokes computations of a stall-regulated wind turbine using low mach number preconditioning". In 44th AIAA Aerospace Sciences Meeting and Exhibit, Reno, Nevada.

[31] Pape, A. L., and Lecanu, J., 2004. "3D navier–stokes computations of a stall-regulated wind turbine". *Wind Energy,* ***7***(4), pp. 309–324.

[32] Schreck, S., 2012. personal communication. NREL.

[33] Jonkman, J., Butterfield, S., Musial, W., and Scott, G., 2009. Definition of a 5-MW reference wind turbine for offshore system development. NREL/TP-500-38060. Tech. rep., NREL.